Corrosion Behavior of X100 Steel Heat-affected Zone in Acidic Soil Solution

Chenqi Fu, Zhedong Xie[*]

College of Engineering and Technology, Jilin Agricultural University, Changchun Jilin 130118, China
[*]E-mail: xiezhedong09@126.com

At present, the research on X100 steel was mainly focused on the manufacturing technology, mechanical properties and welding process, while the corrosion performance of X100 steel that experienced high temperature and then formed heat-affected zone in the welding process was less studied. Therefore, in this paper, the corrosion characteristics of X100 HAZ in acidic soil solution were studied by metallographic analysis and product film morphology observation, and electrochemical method was used to study the electrochemical corrosion behavior at different pH. The results showed that after immersion for 7 days, due to grain refinement effect, corrosion product film of X100 steel and ICHAZ generated more solid density compared to other organizations, enhanced the relative corrosion resistance. However, the product membranes of CGHAZ and IRCGHAZ were more micro defects, therefore in the late corrosion resistance decreased. The results of electrochemical experiments showed that the electrode reaction was controlled by cathode. The electrochemical reaction rate mainly depended on the film structure of corrosion products.

1. INTRODUCTION

The concept of low-alloy high-strength steel was first proposed by the United States in 1934 [1-3]. It referred to the high strength structural steel developed by adding a small amount of alloying elements to ordinary carbon steel [4]. From 70s to 80s in the 20th century, a wave of new pipeline steel research on micro-alloying principle control and cooling technology was formed. In recent years, the manufacturing technology of ultra-high strength pipeline steel (X100) had gradually improved [5,6]. By adding Cu, Ni, Cr and other alloys for matrix strengthening, online forced acceleration of cooling process to promote grain refinement and then improving the degree of homogenization of ferrite matrix, X100 had better welding, brittle fracture resistance, hydrogen sulfide stress corrosion,

hydrogen cracking resistance and other properties [7]. At present, the research on X100 steel was mainly focused on the manufacturing technology, mechanical properties and welding process, while the corrosion performance of X100 steel that experienced high temperature and formed heat-affected zone (HAZ) in the welding process was less studied [8]. Compared with the X100 steel, the microstructure and mechanical properties of HAZ changed. However, there was no unified conclusion on the specific change degree at present [9]. In simulated acid corrosion environment, this paper studied the effect of microstructure of different HAZ of X100 steel on corrosion product film structure, corrosion morphology and the electrochemical characteristics, to explore the characteristics of corrosion and electrochemical corrosion behavior between HAZ groups, which can provide to theoretical support for X100 pipeline steel in the engineering application.

2. EXPERIMENTAL SETTINGS

X100 steel was used as the test material in this paper, and the component was shown in Table 1. The X100 samples with the size of $10.5 \times 10.5 \times 55$ mm^3 were processed for thermal simulation samples by using line-cutting technology. The samples were polished successively with 200#-1200# water sandpaper, and then were pretreated with acetone, anhydrous ethanol. The samples were dried in a vacuum dryer for more than 24 h for reserve.

Table 1. X100 steel composition (mass fraction, wt.%)

Element	C	Si	Mn	P	S	Ni	Cr	Nb	Mo
Wt.%	0.043	0.23	1.86	0.0084	0.0016	0.46	0.21	0.038	0.29

In this paper, the Gleeble 3500 thermal-force simulation machine was used to form the HAZ. The intercritical-gained heat-affected zone (ICHAZ), fine-gained heat-affected zone (FGHAZ) and coarsel-gained heat-affected zone (CGHAZ) were obtained by setting different welding thermal simulation parameters. Considering the multilayer-pass welding, intercritical-reheated coarsel-gained heat-affected zone (IRCGHAZ) and subcritical coarsel-gained heat-affected zone (SCCGHAZ) were constructed by increasing the number of thermal cycles [10-14].

Metallographic experiment. After thermal cycling, the sample was processed into the working sample with the size of $10 \times 10 \times 2$ mm^3. The sample was compacting with thermosetting material and heated at constant temperature for 8 min. The working face was polished successively with 200#-1200# water sandpaper, and then etched with 5% nitric acid alcohol for reserve. Leica DM2500M metallographic microscope was used for metallographic observation, and the differences of microstructure characteristics in different heat-affected zones were analysed.

Immersion experiment. The sample was immersed in simulated soil solution for 7 days. Scanning electron microscopy (SEM) was used to observe the microstructure of the corrosion product film.

Electrochemical experiment. The sample was cleaned by acetone and absolute ethyl alcohol, and then dried for reserve. Before the test, a wire was welded on the back of the sample and epoxy resin was used for packaging. A standard three-electrode system was used to carry out electrochemical experiments, in which the working electrode (WE) was the X100 samples (including HAZ samples), the auxiliary electrode (AE) was platinum electrode, and the reference electrode (RE) was saturated calomel electrode (SCE). The frequency range of electrochemical impedance scanning (EIS) was 10^{-2}-10^5 Hz, the potential scanning range was set to ±250 mV (relative to open circuit potential), and the scanning rate was 0.3 mV/s [15].

The soil simulated solution was prepared by analytical pure chemical reagent and deionized water to simulate acid environment, which chemical composition was $CaCl_2$ 0.111 g/L, NaCl 0.468 g/L, Na_2SO_4 0.142 g/L, $MgSO_4 \cdot 7H_2O$ 0.197 g/L, KNO_3 0.293 g/L, $NaHCO_3$ 0.151 g/L. Glacial acetic acid and NaOH solution were used to adjust the pH value of the simulated solution [16]. The experimental temperature was set at 20°C.

3. RESULTS AND DISCUSSION

3.1 Metallographic analysis

Figure 1 was the metallographic organization morphology of HAZ of X100 steel after etched with 5% nitric acid alcohol.

Figure 1(a) showed the X100 steel without heat treatment. The grain boundary can be vaguely seen in the metallographic morphology, which was a long strip grain. Due to the addition of Mo, Ti and other components to micro-alloying the structure of the X100 steel, the grain was more refined, the microstructure was mainly fine acicular ferrite, strip and granular bainite, irregular polygonal ferrite and flake pearlite [17-19]. A small number of granular M-A components were distributed at the boundary of ferrite or ferrite and bainite, and the distribution was not continuous.

After thermal cycle at 800°C, ICHAZ microstructure was formed, as shown in Figure 1(b). Incomplete phase transition happened in the process of thermal simulation, in which phase change and recrystallization occurred in some tissues. A part of austenite was preferentially nucleated on the original austenite grain boundary, and the original grain boundary was swallowed, which made the grain distribution more discrete. And the microstructure grains were generated by the high temperature reverse microstructure [20]. However, the variation range was small, and there was a phenomenon of mixing of fine and coarse tissues. The two kinds of structures also had polygons, acicular ferrite and granular bainite. The M-A components formed by the reverse structure were all clustered at grain boundaries, but small and dispersed [21]. The austenite tissue with relatively high carbon content underwent complex transformation during continuous cooling, resulting in the black etched area.

FGHAZ was formed when the thermal simulation temperature reached 1050°C, as shown in Figure 1(c). The grain size of FGHAZ was about 10 μm, and the internal structure of FGHAZ was mostly massive ferrite, including fine granular bainite (about 1-2 μm). FGHAZ was in lower higher hardness of the lath structure. After the original austenite grain boundary nucleation, growth will cross

the original austenite grain boundary, make its be overwritten after formation of polygonal ferrite, with coarse border, irregular shape, fuzzy multilateral boundary, mixed with small black etching area. Meanwhile, because the faster cooling rate, M-A components existed in the interior and boundary of granular bainite.

CGHAZ was formed at the high temperature of 1350℃, as shown in Figure 1(d). At this time, the welding thermal simulation temperature was close to the solid phase line temperature of X100 steel, and the austenite grains grew abnormally in the range of 60-100 μm, resulting in the local embrittlement of CGHAZ. Organization form was close to lath martensite and the original austenite grain boundary was clearly visible, in which the stability of supercooled austenite transformation and non-equilibrium transformation product in low temperature all increased [22,23]. Meanwhile, there were more thin film-strip coarse M-A components between the lath, and some granular bainite existed in the grain.

The microstructure morphology of the secondary thermal cycle was closely related to the primary thermal cycle after 1350℃, but more austenite-ferrite grain boundaries were formed. The tissues after the primary thermal cycle had more lath martensite, and then underwent the secondary thermal cycle with T_{max}=800℃ to form IRCGHAZ, as shown in Figure 1(e). IRCGHAZ grain grew up obviously, which can reach about 150 μm. The grain boundary was small, and existed continuous distributed more bulky M-A components along grain boundary, showing the "genetic" phenomenon. It appeared around the proto-austenite grain boundary in the form of discontinuous reticular form, which was chain structure of proto-austenite boundary formed by the participation of M-A components [24]. The internal structure of the grain was similar to that of the CGHAZ, which was composed of lamellar martensite, granular and coarse lath bainite.

SCCGHAZ was formed by secondary thermal cycle with T_{max}=1050℃ based on CGHAZ, as shown in Figure 1(f). The formed austenite recrystallization occurred due to the cold work hardening of phase transformation, and the austenite grains were obviously refined. At this time, the toughness of the structure was improved. Due to the sufficient diffusion of carbon, M-A components and granular bainite structure were formed near the grain boundary and subgrain boundary after cooling. The uneven structure of bainite ferrite, M-A component and granular bainite was formed, and the chemical composition was not eliminated by welding heat treatment [25].

(a) X100 steel   (b) ICHAZ   (c) FGHAZ

(d) CGHAZ   (e) IRCGHAZ   (f) SCCGHAZ
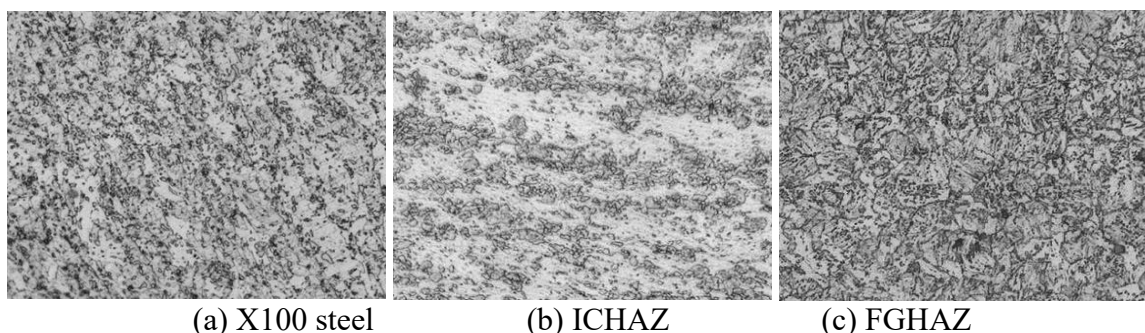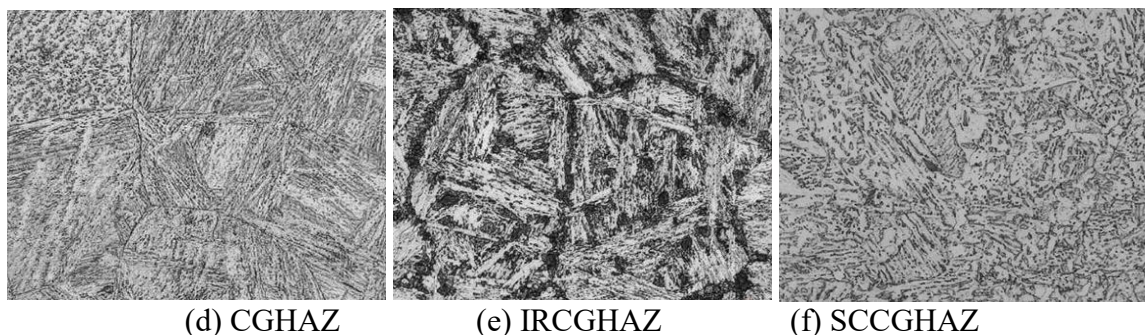
Figure 1. Metallographic organization morphology of HAZ (including X100 steel, ICHAZ, FGHAZ, CGHAZ, IRCGHAZ and SCCGHAZ) after etched with 5% nitric acid alcohol

3.2 Analysis on structure of corrosion product film

SEM corrosion morphology of X100 steel in different heat-affected zones after immersion for 7 days was observed, as shown in Figure 2. The corrosion products of X100 steel were denser. However, in acid simulated solution, the dissolution of the corrosion product film led to the formation of gully fine lines on the surface of the film, which had little influence on the protection of the product film. These characteristics hindered the infiltration of corrosive ions into the matrix in the corrosive medium, which can slow down the corrosion degree of X100 steel [26-29]. In addition, the short rod-shaped α-FeO(OH) was visible on the surface of the product film, which was a thermodynamically stable state of FeO(OH). The hindrance effect of the structure on the erosive ions was weak and could be ignored.

The corrosion product stricture of ICHAZ was similar to that of X100 steel, showing a dense structure with fine cracks. For another aspect, product shedding phenomenon occurred locally, and there were large but shallow holes on the surfac. It can be seen from the holes that the inner film was formed by the accumulation of granular products. The overall product film structure had poor stability compared with the X100 steel, leading to a decrease in the protection degree. However, compared with the product film of other tissues, its protection was still at a high level.

FGHAZ corrosion product film covered with a flocculent organization was rough, in which this kind of organization was unable to protect the matrix. A flat dense membrane under flocculent organization was formed, while there were relatively bulky reticular crack defects on the outer membrane [30,31]. Furthermore, the cracks continued to expand until local stratification occurred on the product film, exposing the block structure of the inner film, which made corrosive ions in the solution easily pass through the microscopic channels of the crack defect in the product film and then destroyed the matrix.

The surface of CGHAZ corrosion product was covered with petal-like reddish-brown α-FeO(OH) corrosion product, showing a cluster, loose and porous structure, which had no protective effect on the matrix. There were many microscopic defects in the outer membrane, and the defects gradually developed into gullies, exposing the inner membrane structure with irregular gully lines. The morphology and distribution of the product film provided conditions and channels for the corrosive ions to penetrate into the matrix and then accelerated the corrosion process.

IRCGHAZ was the structure with the largest grains and the most obvious grain boundaries. Its corrosion products showed obvious large-scale shedding and uneven phenomenon, forming a large low-lying platform. The film of residual corrosion products was loose, with a large number of defects and poor compactness [32]. The exposed surface showed small radial gullies, and the stability of the film was poor, which weakened the binding force between the film layer and the matrix.

The surface of SCCGHAZ corrosion product was a layer of loose and porous stacking structure, which made the surface of the corrosion product uneven and affected the uniformity and compactness of the surface morphology. The structure had a certain blocking effect on the corrosive anions in the simulated solution, but due to the high density of the pores, the ions will carry out material transfer through the pores and accelerate the activation and dissolution of the matrix, so the protection effect was not strong and the corrosion rate was larger.

| (a) X100 steel | (b) ICHAZ | (c) FGHAZ |
| (d) CGHAZ | (e) IRCGHAZ | (f) SCCGHAZ |
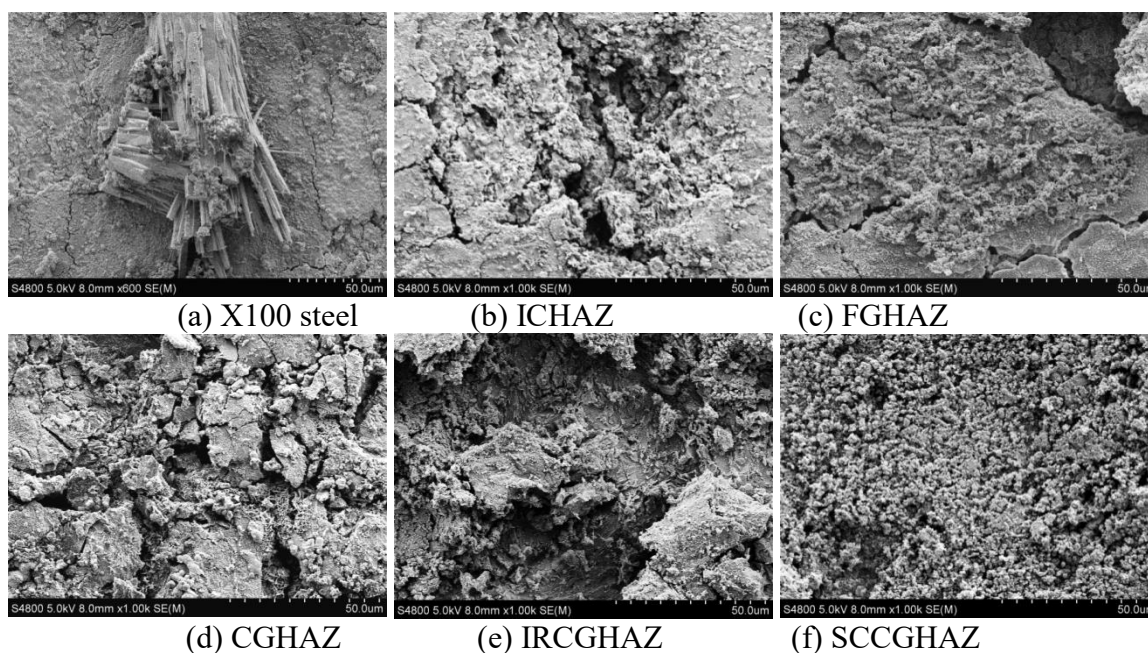
Figure 2. Corrosion product morphology of different HAZ (including X100 steel, ICHAZ, FGHAZ, CGHAZ, IRCGHAZ and SCCGHAZ) after immersed in simulated soil solution for 7 days at 20°C

3.3 Analysis on electrochemical test

3.3.1 Analysis on polarization curve

Figure 3 showed the polarization curves of the heat-affected zone at different pH values. At pH=2.4, polarization curves of different HAZ were relatively similar, and showed a cathodic control process. The corrosion products in strong acidic corrosive medium were easily dissolved, in which no passivation occurred and the anodic polarization zone showed obvious Tafel characteristics. When the pH was increased to 3.6, the corrosion current decreased greatly, and a relatively obvious Tafel region

appeared in the anodic polarization region, showing an activation control. The polarization potential of IRCGHAZ and SCCGHAZ increased while the current decreased during cathodic polarization, which was similar to the "passivation transition zone" of anode. Because the corrosive medium was still in a strong acidic environment, it was difficult for the sample matrix to produce protective passivation film, and the characteristics of the tissue itself had a great influence on the corrosion resistance. At pH=4.2, the electrode process changed greatly [33]. On the one hand, the corrosion current density decreased with the increase of pH. On the other hand, it was related to the deposition of corrosion products on the surface of electrode tissue. At this time, due to local super-saturation of Fe^{2+} generated by anodic dissolution, the passivated corrosion products were covered by the electrode surface, which inhibited the anodic dissolution process. At pH=5.5, Tafel region existed in the polarization curve of all samples, and the anodic reaction was controlled by activation. At this time, H^+ content in the solution was relatively little, and the solution was weak acidic [34]. The corrosion potential and corrosion current density had little difference compared with pH=4.2. The influence of pH value on the system was very small, indicating that the anodic dissolution rate decreased significantly. The X100 steel and ICHAZ still showed relatively excellent corrosion resistance.
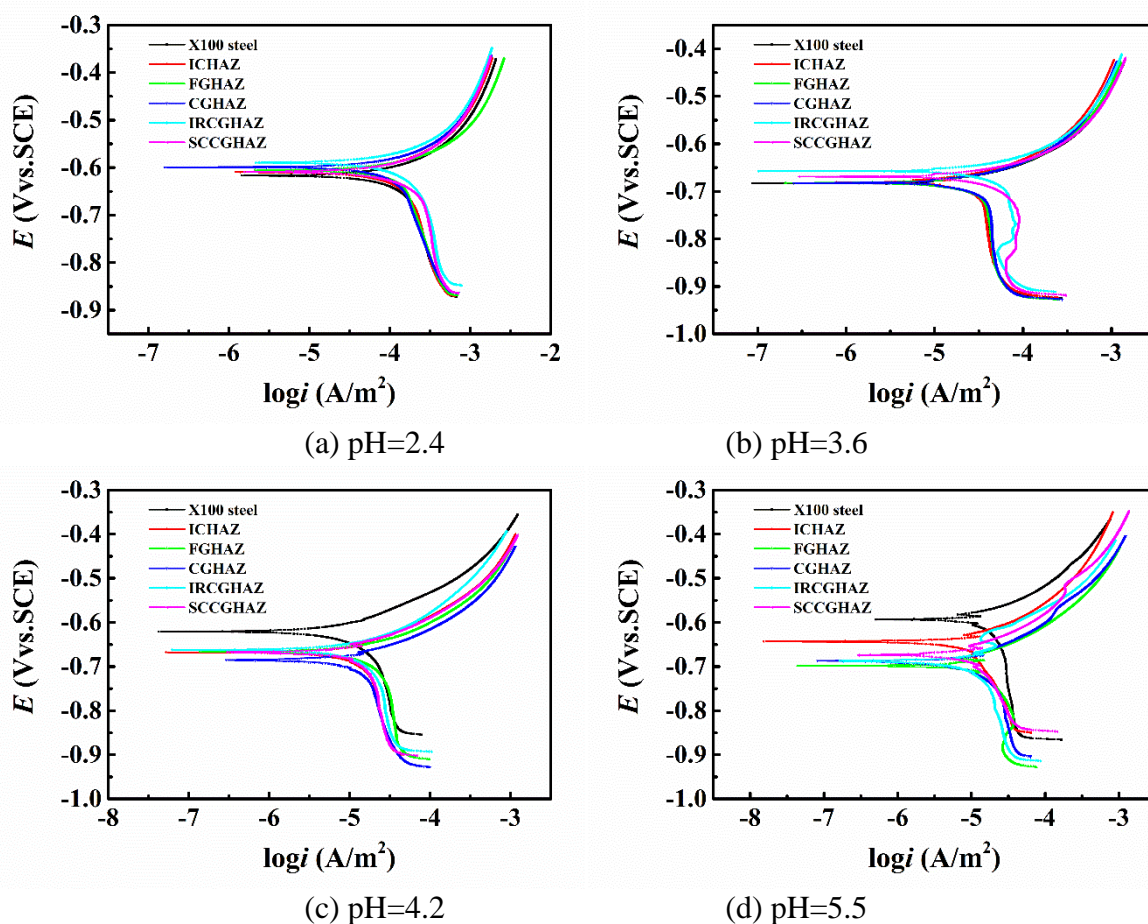
Figure 3. Polarization curves of different HAZ (including X100 steel, ICHAZ, FGHAZ, CGHAZ, IRCGHAZ and SCCGHAZ) at different pH (including 2.4, 3.6, 4.2 and 5.5) with experimental temperature of 20°C

Table 2 showed the corrosion potential (E_{corr}) and corrosion current density (I_{corr}) of polarization curves for different HAC of X100 steel at different pH. When the corrosive medium was more acidic (pH=2.4), the thermodynamic corrosion tendency was the largest, and the corrosion rate was also high. According to the fitting data in the table, IRCGHAZ with large grains and obvious grain boundary had the lowest corrosion current density (only 73.33 mA/cm^2), followed by CGHAZ with slightly fine grained boundaries. The corrosion current density of the other four kinds of tissues with no obvious grain boundaries had little difference (about 100 mA/cm^2). With the increase of pH (pH=3.9), CGHAZ and IRCGHAZ still had lower corrosion current density and better corrosion resistance. At pH=4.6, the H$^+$ content in the corrosion medium decreased, and corrosion product film was formed on the surface, which had a certain protective effect on the matrix. At this time, the X100 steel and ICHAZ showed excellent corrosion resistance [35]. Combined with the analysis of the membrane structure of the corrosion products, it can be seen that the CGHAZ and IRCGHAZ were not conducive to the close adsorption of corrosion products, resulting in large defects and reduced corrosion resistance. Especially, the I_{corr} of IRCGHAZ was as high as 17.16 mA/cm^2, which was significantly higher than other structures. When the corrosive medium was nearly neutral or weakly acidic aqueous solution (pH=5.5), the main factors affecting the corrosion rate were the protective effect of the film formed by the deposition of corrosion products on the tissue surface and the difficulty of oxygen in the medium to reach the cathode surface. The difference of corrosion current density was small, but the X100 steel still had a slightly better corrosion resistant performance [36]. It was due to that grain refinement can decrease the number of cracks in the corrosion product film and corrosion holes, make product attached more densely, and then improve the protection of matrix.

Table 2. The corrosion potential (E_{corr}) and corrosion current density (I_{corr}) of different HAZ (including X100 steel, ICHAZ, FGHAZ, CGHAZ, IRCGHAZ and SCCGHAZ) at different pH (including 2.4, 3.6, 4.2 and 5.5) with experimental temperature of 20°C

Parameter	pH	X100 steel	ICHAZ	FGHAZ	CGHAZ	IRCGHAZ	SCCGHAZ
E_{corr} (mV)	2.4	-614	-610	-590	-606	-597	-609
	3.6	-657	-681	-681	-680	-667	-668
	4.2	-620	-665	-663	-683	-595	-665
	5.5	-689	-646	-697	-688	-674	-682
I_{corr} (mA/cm^2)	2.4	96.00	98.38	104.90	94.95	73.33	106.40
	3.6	39.54	23.50	22.74	18.57	13.11	40.74
	4.2	8.32	9.26	11.07	12.21	17.16	10.57
	5.5	7.98	9.12	10.23	10.72	12.66	9.58

3.3.2 Analysis on EIS

Figure 4 showed EIS curves of heat-affected zone at different pH. At pH=2.4, the EIS curves of different HAZ had similar variation trends, and they were all composed of double capacitive reactance arcs and low frequency inductive reactance arcs. The high frequency capacitive arc was related to the corrosion reaction, while the low frequency capacitive arc was related to the double layer. The contact surface between the HAZ of X100 steel and the corrosive medium can be divided into two parts: one

was the formation of dense corrosion product film, and the other part was that due to the occurrence of intergranular corrosion, the corrosion medium contacted the exposed grain boundary of the tissue. Due to the acidic environment, intergranular corrosion can easily occur in the tissue matrix, and pitting nucleation led to the formation of low-frequency inductive reactance arcs [37]. At pH=3.6, the difference in microstructure only affected the capacitive reactance arc and inductive reactance arc, indicating that only the electrode reaction rate in the system was changed, but the electrochemical reaction was same.
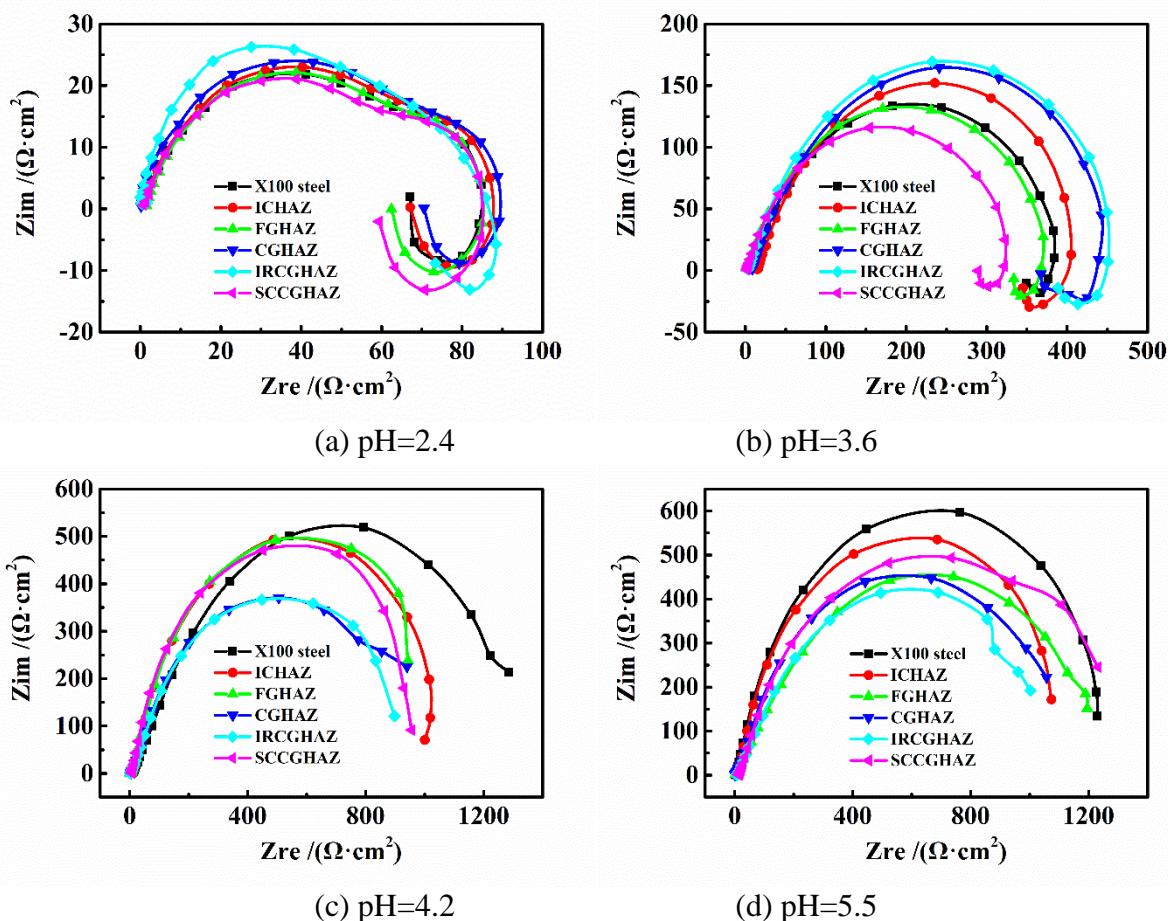
Figure 4. EIS curves of different HAZ (including X100 steel, ICHAZ, FGHAZ, CGHAZ, IRCGHAZ and SCCGHAZ) at different pH (including 2.4, 3.6, 4.2 and 5.5) with experimental temperature of 20°C

The low-frequency inductive reactance arc was caused by the uneven reaction caused by the continuous adsorption and desorption on the tissue surface due to the strong acidity of the solution and the difficulty of film formation of the corrosion products. At pH=4.2, the EIS showed the single capacitive arc reactance, which was mainly controlled by activation and reflected the transmission process of charge or other substances involved in the reaction through the product film. At this time, the damage effect of pH on the product film was reduced, and the protective effect of the film had a

great influence on the corrosion resistance of the tissue [38]. At pH=5.5, the EIS of different HAZ of X100 steel only showed the arc resistance characteristics, which was similar to the impedance characteristics at pH=4.2, indicating that they had the same corrosion reaction process. In this case, the radius of arc was as follows: X100 steel > ICHAZ > SCCGHAZ > FGHAZ > CGHAZ > IRCGHAZ. With the reduction of arc radius, the resistance to electrode reaction weakened, the corrosion current increased, and the corrosion rate increased.

Tab.3 showed the fitted results of EIS curves of heat-affected zone at different pH. At pH=2.4, the charge transfer resistance (R_{ct}) of IRCGHAZ was 70.89 $\Omega \cdot cm^2$, slightly higher than that of other tissues, showing good corrosion resistance, which was consistent with the polarization curve results. This was because the solution was acidic, the surface of IRCGHAZ was in active corrosion state, and various trace alloying elements were concentrated at the grain boundary, which made the potential at the grain boundary more negative than that in the grain boundary and became the pitting area. At this time, the grains of IRCGHAZ became larger due to thermal cycling, and the proportion of grain boundaries was small [39,40]. The atomic energy within grain boundaries was lower than that at grain boundaries, and the number of active atoms involved in corrosion decreased, which reduced the reaction activity, and then reduced the corrosion rate, effectively alleviating the corrosion degree and improving the corrosion resistance of steel. The R_{ct} of SCCGHAZ was only 57 $\Omega \cdot cm^2$, which may be caused by the formation of uneven structure of bainite ferrite, M-A components and granular bainite, reducing the stability of the tissue itself. At pH=3.6, the EIS deviated from the semicircle trajectory, with "dispersion effect", and the radius of capacitive reactance arc was as follows: IRCGHAZ > CGHAZ > ICHAZ > X100 steel > FGHAZ > SCCGHAZ, that is, the arc radius of the microstructure of the X100 steel and ICHAZ with large grains and obvious grain boundaries was larger than that of the X100 steel and ICHAZ with fine grains. The arc radius of the microstructure of the X100 steel and ICHAZ with large grains but no obvious grain boundaries was the smallest. By comparing the R_{ct} of HAZ, IRCGHAZ had the largest R_{ct} of 383.1 $\Omega \cdot cm^2$, while SCCGHAZ had the worst corrosion resistance. At pH=4.2, the corrosion resistance of X100 steel with grain refinement had obvious improvement.

Table 3. The fitted results of double-layer capacity (C_{dl}) and charge transfer resistance (R_{ct}) of different HAZ (including X100 steel, ICHAZ, FGHAZ, CGHAZ, IRCGHAZ and SCCGHAZ) at different pH (including 2.4, 3.6, 4.2 and 5.5) with experimental temperature of 20℃

pH	Parameter	X100 steel	ICHAZ	FGHAZ	CGHAZ	IRCGHAZ	SCCGHAZ
2.4	C_{dl} (F·cm^{-2})	5.699×10^{-4}	5.346×10^{-4}	5.729×10^{-4}	5.928×10^{-4}	5.028×10^{-4}	5.034×10^{-4}
	R_{ct} (Ω·cm^2)	65.96	61.65	61.14	66.51	70.89	57.00
3.6	C_{dl} (F·cm^{-2})	3.655×10^{-4}	3.566×10^{-4}	3.995×10^{-4}	4.061×10^{-4}	4.021×10^{-4}	3.975×10^{-4}
	R_{ct} (Ω·cm^2)	324.00	338.20	323.60	367.00	383.10	286.10
4.2	C_{dl} (F·cm^{-2})	1.736×10^{-3}	5.657×10^{-3}	1.64×10^{-3}	8.683×10^{-4}	1.173×10^{-3}	1.83×10^{-3}
	R_{ct} (Ω·cm^2)	1245	1072	1052	1027	920.6	1039
5.5	C_{dl} (F·cm^{-2})	1.644×10^{-3}	6.813×10^{-4}	1.875×10^{-3}	1.11×10^{-3}	1.539×10^{-3}	1.228×10^{-3}
	R_{ct} (Ω·cm^2)	1379	1326	1225	1223	1168	1312

Due to the weak acidic simulation solution, the distribution of corrosion product was uniform, and a relatively stable membrane was generated to protect the matrix. Although ICHAZ also had grain refinement, its grain dispersion was not uniform, which affected the dense adsorption of product film. However, on the whole, R_{ct} of ICHAZ was still at a high level with excellent corrosion resistance. However, the grains of CGHAZ and IRCGHAZ that underwent high temperature thermal cycle were coarse, and the corrosion products covered by the surface had many microscopic defects, which reduced the corrosion resistance. The R_{ct} of IRCGHAZ in acidic simulated solution at pH=4.7 was only 920.6 $\Omega \cdot cm^2$. At pH=5.5, compared with pH=4.7, R_{ct} did not improve greatly, and the X100 steel and ICHAZ still showed good corrosion resistance. X100 steel and ICHAZ structure at pH=5.5 was weaker, and the corrosion was relatively light.

4. CONCLUSION

In this paper, the different HAZ of X100 steel were obtained by Gleeble 3500 thermal-force simulation machine, and the corrosion behavior in simulated acidic solution was studied. The following conclusions were drawn.

(1) Through the analysis of metallographic structure and product film morphology, it can be found that the grain boundaries of CGHAZ and IRCGHAZ were relatively small, and the corrosion resistance was the best. Corrosion product film had a greater influence on the performance of corrosion characteristic. Due to grain refinement effect, corrosion product film of X100 steel and ICHAZ generated more solid density compared to other organizations, enhanced the relative corrosion resistance. However, the product membrane of CGHAZ and IRCGHAZ was more micro defects, therefore in the late corrosion resistance decreased.

(2) The results of electrochemical experiments showed that the anode reaction was controlled by activation and the electrode reaction was controlled by cathode. The EIS curves of the HAZ of X100 steel can be divided into two cases. In the first case, the low-frequency area was characterized by inductive reactance, and the microstructure surface of the HAZ was in a state of active dissolution without product precipitation. At this time, the microstructure corrosion degree of the SCCGHAZ was the most serious. In the second case, the EIS only showed the characteristic of single arc, reflecting the formation of the corrosion product layer on the electrode surface. In this case, the CGHAZ and the SCCGHAZ had poor corrosion resistance.

References

1. D.X. Xia, X.L. Wang, X.C. Li, Y. You and C.J. Shan. *Acta Metall. Sin.*, 49 (2013) 271.
2. S.B. Lalvani and G. Zhang. *Corros. Sci.*, 1995, 37(10): 1567-1582.
3. S. Nafisi, B.S. Amirkhiz, F. Fazeli, M. Arafin, R. Glodowski and L. Collins. *ISIJ Int.*, 56 (2016) 154.
4. I.M. Gadala and A. Alfantazi. *Appl. Surf. Sci.*, 357 (2015) 356.
5. M. Witek. *J. Nat. Gas Sci. Eng.*, 27 (2015) 374.

6.　A.Y. Ivanov, R.V. Sulyagin, V.V. Orlov and A.A. Kruglova. *Met. Sci. Heat Treat*., 53 (2012) 560.
7.　A.A. Kruglov, V.V. Orloy, O.V. Sych and E Khlusova. *Metallurgist*. 57 (2013) 113.
8.　Z. Lu, J. Chen, T. Shoji, Y. Takeda and S. Yamazaki. *J. Nucl. Mater*., 465 (2015) 471.
9.　C. Yu, X. Gao and P. Wang. *Electrochemistry*, 83 (2015) 406.
10.　H.H. Huang and W.T. Tsai. *Electrochim. Acta*, 41 (1996) 1191.
11.　L.Y. Xu, J. Yang, R.Z. Wang, W.L. Wang and Y.N. Wang. *J. Iron Steel Res. Int.*, 25 (2018) 433.
12.　J. Moon, H.Y. Ha, T.H. Lee and C. Lee. *Mater. Chem. Phys*., 142 (2013) 556.
13.　J. Laitila, J. Larkiola and D. Porter. *Weld. World*, 62 (2018) 2018.
14.　J. Xiao, T. Xiao, Y.Q. Zheng, H. Wang, Y. Chen, S.Y. Qiu and X. Gong. *J. Nucl. Mater.*, 537 (2020) 152259.
15.　X. Xu and J.A. Siefert, J.D. Parker and R.C. Thomson. *Mater. Design*, 196 (2020) 109046.
16.　C.Q. Ye, R.G. Hu, S.G. Dong, X.J. Zhang and J.S. *Journal of Electroanal. Chem*., 688 (2013) 275.
17.　M. Mobin, A.U. Malik and I.N. Andijani. *Desalination*, 217 (2007) 233.
18.　X. Xi, J. Wang, L. Chen and Z. Wang. *J. Mater. Sci.*, 55 (2020) 10863.
19.　H.N. Lou, W. Chao, B.X. Wang, Z.D. Wang and R.D.K. Misra. *J. Iron Steel Res. Int.*, 26 (2019) 501.
20.　M. Shojaati, S.F.K. Bozorg, M. Vatanara, M. Yazdizadeh and M. Abbasi. *Int. J. Pres. Ves. Pip.*, 188 (2020) 104205.
21.　G.S. Peng, K.H. Chen, H.C. Fang, H. Chao and S.Y. Chen. *Mater. Corros*., 61 (2010) 783.
22.　J. Moon and C. Lee. *Acta Mater*., 57 (2009) 2311.
23.　S.S.M. Tavares, J.M. Pardal, L.D. Lima, I.N. Bastos, A.M. Nascimento and J.A.D. Souza. *Mater. Charact.,* 58 (2007) 610.
24.　G.Z. Wu, K. Ding, S.F. Qiao, T. Wei, X. Liu and Y.L. Gao. *J. Mater. Res. Technol.*, 14 (2021) 2233.
25.　M.N. Julian and M.C. Gupta. *Opt. Laser. Eng.*, 126 (2020) 105911.
26.　A.R. Khan, S. Yu and M. Zubair. *J. Mater. Eng. Perform.*, 30 (2020) 1.
27.　L.W. Wang, Z.Y. Liu, Z.Y. Cui, C.W. Du, X.H. Wang and X.G. Li. *Corros. Sci*., 85 (2014) 401.
28.　F. Mohammadi, F.F. Eliyan and A. Alfantazi, *Corros. Sci*., 63 (2012) 323.
29.　X.W. Lei, S.B. Zhou and J.H. Huang. *Metall. Mater. Trans. A*, 51 (2020) 1665.
30.　J. Gao, Z.Y. Zhang, J.B. Tan, X.Q. Wu, X. Wang, E.H. Han and W. Ke. *Int. J. Fatigue*, 148 (2021) 106223.
31.　G.A. Zhang and Y.F. Cheng, *Corros. Sci*., 51 (2009) 1714.
32.　F.E. Faysal and A. Akram. *Corros. Sci*., 74 (2013) 297.
33.　Z. Zhang, Y. Zhao, J. Shan, A. Wu and X. Tang. *J. Alloy. Compd.*, 863 (2021) 158463.
34.　K. Gong, M. Wu, F. Xie, G. Liu and D. Sun. *Mater. Chem. Phys.*, 270 (2021) 124826.
35.　Y. Kumar, M.K. Dash, A. Moitra, G. Sasikala and S.K. Albert. *Mat. Sci. Eng. A*, 12 (2021) 141180.
36.　W. Zhao, Y. Zou, K. Matsuda and Z. Zou. *Mater. Design*, 99 (2016) 44.
37.　G.C. Savva, G.C. Weatherly and K.T. Aust. *Corrosion*, 45 (2012) 243.
38.　M.H. Chen, R.Y. Hwang and C.P. Chou. *Sci. Technol. Weld. Joi*., 41 (2014) 21.
39.　R. Koňár and M. Patek. *The. Vjesn*., 24 (2017) 137.
40.　X.H. Zhang, S. Pehkonen, N. Kocherginsky and G.A. Ellis. *Corros. Sci*., 44 (2002) 2507.